ACS Catalysis

Research Article

pubs.acs.org/acscatalysis

Facile Fabrication of Composition-Tuned Ru−Ni Bimetallics in Ordered Mesoporous Carbon for Levulinic Acid Hydrogenation

Ying Yang,[†,‡] Guang Gao,[†] Xin Zhang,[‡] and Fuwei Li*[,†]

[†]State Key Laboratory for Oxo Synthesis and Selective Oxidation, Lanzhou Institute of Chemical Physics, Chinese Academy of Sciences, Lanzhou, Gansu 730000, P. R. China

[‡]State Key Laboratory of Heavy Oil Processing, China University of Petroleum, Changping, Beijing 102249, China

Supporting Information

ABSTRACT: Bimetallic catalysts are of great importance due to their unique catalytic properties. However, their conventional synthesis requires tedious multistep procedures and prolonged synthetic time, and the resulting bimetallics usually disperse unevenly and show poor stability. It is challenging to develop a facile and step-economic synthetic methodology for highly efficient bimetallic catalysts. In this study, we report an elegant metal complex-involved multicomponent assembly route to highly efficient Ru−Ni bimetallics in ordered mesoporous carbons (OMC). The fabrication of composition-tuned Ru−Ni bimetallics in OMC (Ru_xNi_{1-x}−OMC, x = 0.5−0.9) was facilely realized via in situ construction of CTAB-directed cubic *Ia*3*d* chitosan-ruthenium−nickel−silica mesophase before pyrolysis and silica removal. The resulting Ru_xNi_{1-x}−OMC materials are in-depth characterized with X-ray diffraction, N_2 adsorption−desorption, transmission electron microscopy, infrared spectrum, and X-ray absorption fine structure. This facile fabrication method renders homogeneously dispersed Ru−Ni bimetallics embedded in the mesoporous carbonaceous framework and creates a highly active and stable $Ru_{0.9}Ni_{0.1}$−OMC catalyst for the hydrogenation of levulinic acid (LA) to prepare γ-valerolactone (GVL), a biomass-derived platform molecule with wide application in the preparation of renewable chemicals and liquid transportation fuels. A high TOF (>2000 h^{-1}) was obtained, and the $Ru_{0.9}Ni_{0.1}$−OMC catalyst could be used at least 15 times without obvious loss of its catalytic performance.

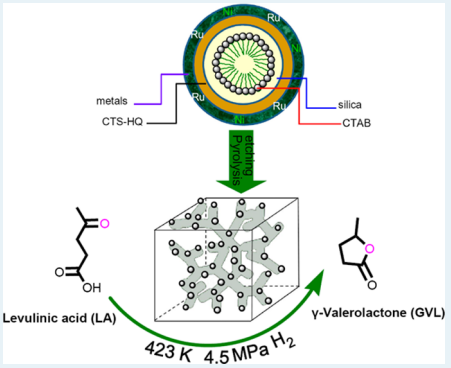

KEYWORDS: *embedded bimetallics, ordered mesoporous carbon, pyrolysis, self-assembly, levulinic acid hydrogenation, high stability*

1. INTRODUCTION

Bimetallics are of great importance owing to their tunable composition, size, and electronic properties linked to various applications including magnetism, electronics, photonics, and especially catalysis.[1−4] To construct durable bimetallic catalysts, two metals are commonly dispersed onto porous carbons to prepare heterogeneous bimetallic catalysts, benefiting from the wide adaptability of chemically inert and (hydro)thermally stable carbons in various harsh conditions.[5] Mesoporous carbons are much favored since they offer great advantages over conventional activated carbons (AC) owing to their well-controlled mesopore structures which are favorable to transportation of the substrate and product.[6] Recent advances in the fabrication of bimetallic mesoporous carbons focus on preconstruction of mesoporous carbon by a hard-templating approach before metal impregnation and reduction, or preformation of bimetallics stabilized by protecting agents before anchorage.[7−9] However, such postsynthetic methods usually created weakly attached bimetallics that were unevenly distributed on the hydrophobic carbons, leading to easy particle aggregation and catalyst leaching.[10] It is known that the catalytic performance of supported bimetallics is highly sensitive to the nanoparticle (NP) dispersion and composition, as well as its affinity to the mesoporous supports, which depends greatly on the synthetic methodology. Despite continuous efforts, the facile fabrication of homogeneously dispersed bimetallics firmly embedded in ordered mesoporous carbons via a step-economic route still remains a challenge.

Catalytic conversion of levulinic acid (LA) to γ-valerolactone (GVL) plays a key role in low-carbon and sustainable biomass conversion; GVL can be widely used as a fuel additive, food ingredient, and intermediate for fine chemical production.[11,12] For this process, studies have shown that traditional Ru/C is one of the most active heterogeneous catalysts; however, its easy aggregation and leaching leading to low stability is still a concern.[13,14] Ruthenium with oxophilic metal twining hydrogenation catalysts, such as composition-tuned Ru_3Re_4/C and $Ru_{3.6}Sn_1$/C, displayed improved stability in the presence of sulfuric acid and alkylphenol solvent.[15,16] However, both ruthenium-containing bimetallic carbons also face the dilemma of tedious multistep synthesis and the corresponding limited performance owing to the unevenly dispersed NPs and their

Received: November 6, 2013
Revised: March 24, 2014
Published: March 25, 2014

   dx.doi.org/10.1021/cs401030u | ACS Catal. 2014, 4, 1419−1425

weak affinity with AC. Evidently, such a dilemma could be overcome by renovating the ruthenium-containing bimetallic mesoporous carbon design.

From the latest research on the carbon supported metal catalysts, we know that direct pyrolysis of metal coordination polymers or metal organic frameworks under an inert atmosphere can afford homogeneously dispersed metal NPs firmly embedded in a carbonaceous matrix.[17,18] However, owing to the uncontrollable transformation of flexible precursor compounds during pyrolysis, the resulting carbonaceous frameworks are always disordered and microporous. Construction of ordered mesoporous carbons has been well demonstrated by the pyrolysis of self-assembled block copolymer templates and polymerizable precursors recently.[19−22] Inspired by the advantages of the both methodologies and as our continuing interest in the development of nanoparticle catalysts supported on the functional carbons,[17,23] we hypothesize that pyrolysis of surfactant-templated metal coordination polymers may in situ fabricate homogeneously dispersed metal NPs firmly embedded in ordered mesoporous carbons. A polymerizable precursor possessing excellent chelation with metals is the key to realizing this design, since present polymerizable precursors, like phenolic resin and its derivatives,[24] are hard to chelate metal ions to form metal coordination polymers due to the absence of chelating sites. It is known that chitosan is a very abundant biodegradeble and biocompatible polysaccharide obtained by the alkaline deacetylation of chitin[25] and possesses rich hydroxyl and amine moieties with strong affinity for metal ions.[26] Therefore, it is speculated that chitosan may be a suitable chelating agent for constructing metal coordination polymers.

We herein report in situ fabrication of composition-tuned Ru−Ni bimetallic mesoporous carbons by constructing cubic *Ia*3*d* chitosan−ruthenium−nickel−silica mesophase via CTAB-directed self-assembly of different proportions of ruthenium chloride and nickel acetate with 8-quinolinol modified chitosan (CTS-HQ) before pyrolysis and silica removal. This facile route renders homogeneously dispersed Ru−Ni bimetallic NPs inside the ordered mesoporous carbons without using any stabilizer and additional reductant and was confirmed by various characterization techniques. For catalytic hydrogenation of levulinic acid, composition tunable $Ru_{0.9}Ni_{0.1}$−OMC exhibits the highest TOF value (2191 h^{-1}) and stability (15 times recyclability) of the reported bimetallic catalysts.

2. EXPERIMENTAL SECTION

2.1. Sample Preparation. The synthetic procedures for Ru−Ni bimetallic mesoporous carbons are depicted in Scheme 1. Because chitosan only dissolves in acidic solvents such as HCl aqueous solution or acetic acid, to enhance its solubility under the hydrothermal synthesis conditions and coordination ability with the meal precursors, the chitosan was first modified by reaction with 5-chloromethyl-8-quinolinol to afford 8-quinolinol modified chitosan, CTS-HQ, involving a two-step chemical transformation from 8-quinolinol (see Supporting Information and Figures S1−S5). Then, the precursor composite, Ru_xNi_{1-x}−C_{16}SC, was prepared by CTAB-directed self-assembly of different proportions of $RuCl_3{\cdot}nH_2O$ and $Ni(CH_3COO)_2{\cdot}4H_2O$ with CTS-HQ under a basic medium. The molar ratio of the precursor gels used in the preferred preparation is 0.12 CTAB/8.0 NH_3 (25 wt %)/114 H_2O/10 EtOH/1 TEOS/0.5 CTS-HQ/0.625 M (M = Ru_xNi_{1-x}), where x was set as 0.5, 0.7, and 0.9. After the mixture was stirred at

Scheme 1. Synthesis of Ru_xNi_{1-x}−OMC Catalysts

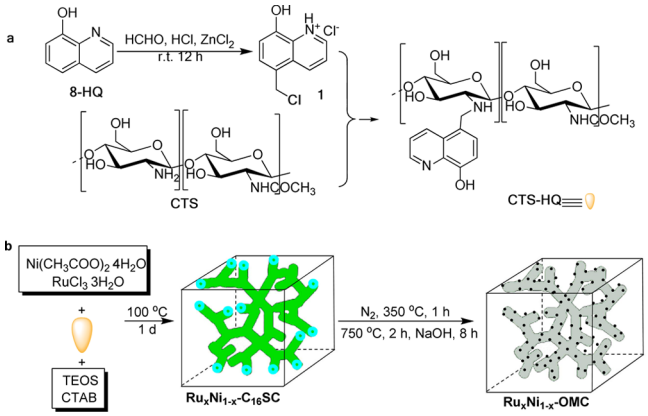

room temperature for 2 h, the resulting gel was transferred to a polyethylene container and heated at 100 °C for 1 day. The as-made product was washed, dried, and pyrolyzed in a tubular furnace under a N_2 atmosphere. The heating rate was 2 °C/min below 350 and 5 °C/min above 350 °C, and pyrolysis was carried out at 750 °C for 2 h. The resulting solid with different compositions was denoted as Ru_xNi_{1-x}−OMSC and subjected to alkaline etching with 3.0 M NaOH solution to remove silica layers, affording Ru_xNi_{1-x}−OMC.

2.2. Material Characterization. Powder X-ray diffraction (XRD) was collected with a Bruker D8 Advance X-ray diffractometer with nickel filtered Cu Kα radiation (λ = 1.5406 Å). The samples were scanned in the range 2θ = 1.2−10.0° and in steps of 2°/min. Morphology and microstructure of Ru_xNi_{1-x}−OMC series were analyzed using a FEI Tecnai G2 F20 transmission electron microscope (TEM) equipped with an energy dispersive X-ray spectroscopic analyzer operated at a voltage of 200 kV. Samples were sonicated for 5 min in EtOH; one drop of the suspended sample was dripped in a holely carbon film supported on a 300 mesh copper grid. N_2 adsorption/desorption isotherms were recorded at 77 K with a Micromeritics Tristar II 3020. Before measurements, the samples were outgassed at 300 °C for 3 h. The specific surface area was calculated by using the Brunauer−Emmett−Teller (BET) method, and the pore size distributions were measured by using Barrett−Joyner−Halenda (BJH) analysis from the desorption branch of the isotherms. Synchrontron X-ray diffraction measurements were performed at the 11-ID-C beamline of the Advanced Photon Source (APS) at Argonne National Laboratory. High-energy X-rays of 115 keV energy and 0.6 mm × 0.6 mm beam size were used to obtain two-dimensional (2D) diffraction patterns in the transmission geometry using a Perkin-Elmer large area detector placed at 1.6 m from the sample. X-ray absorption fine structure (XAFS) was carried out on a beamline at the 20-ID and 20-BM at APS at Argonne National Laboratory. The XAFS data were obtained in the transmission mode at the Ni K-edge (8333.0 eV) and Ru K-edge (22117.0 eV). Other relative information and characterization techniques can be found in the Supporting Information in detail.

Metal content was estimated by inductively coupled plasma atomic emission spectroscopy (ICP-AES) analysis conducted on a Perkin-Elmer emission spectrometer. Each 10 mg sample of vacuum-dried material was placed in a PTFE lined digester and dissolved in 5 mL of boiling aqua fortis solution. Microwave digestion was carried out for 10 min to completely

dx.doi.org/10.1021/cs401030u | ACS Catal. 2014, 4, 1419−1425

dissolve the metal species. After cooling, each solution was filtered through a 0.45 μm polyethersulfone filter and then submitted for metal analysis.

2.3. Catalytic Test. The LA hydrogenation reactions were carried out in a 100 mL magnetically stirred Parr 4560 autoclave equipped with a P.I.D. controller 4843. In a typical procedure, 15 mg of catalyst and 5.0 g of LA were introduced into the autoclave. The sealed autoclave was charged and deflated with N_2 three times before it was pressurized with H_2 to 4.5 MPa at room temperature and heated at 150 °C for a certain reaction duration. Then, the reactor was cooled with cold water, the reaction mixture was centrifugated, and the solid catalyst was washed and could be directly used for the next cycle. The separated liquid reaction solution was quantitatively analyzed with Agilent 6820 gas chromatography using toluene as an internal standard.

3. RESULTS AND DISCUSSION

In this study, chitosan was first modified by 5-chloromethyl-8-quinolinol to enhance its chelation with metal ions and interaction with surfactant CTAB *via* electronic attraction in the aqueous phase, facilitating the formation of a CTAB-directed cubic *Ia*3*d* chitosan−ruthenium−nickel−silica mesophase. During the self-assembly process, CTS-HQ not only binds and disperses metals well in sol−gel process but also interacts with positive CTA+ to enlarge the surfactant hydrophobic volume, rendering a decrease in micelle curvature to form cubic a *Ia*3*d* mesophase along with silica (Figure S6).[27−29] Owing to the difference in chemical and thermal stability between chitosan and surfactant CTAB, as well as the reducibility of carbons, the following pyrolysis is a unique "one stone, three birds" strategy to remove CTAB, carbonize CTS-HQ, and reduce metal ions in a single step. During pyrolysis, silica framework acts as a hard template to consolidate the cubic *Ia*3*d* structure, and its removal affords replicated intercrossed carbonaceous mesopores with large surface areas and pore volumes.

$Ru_{0.9}Ni_{0.1}$−containing samples are chosen as representatives for structural, spectroscopic, and textual property studies, since the same transformation occurs over different Ru_xNi_{1-x}−C_{16}SC samples. Small angle X-ray diffraction patterns clearly reveal the cubic *Ia*3*d* featured (211), (220), (321), (400), and (420) diffractions in the 2θ range from 2 to 5°,[30,31] except for shift toward higher 2θ values that occurred after pyrolysis, linking to lattice contraction (Figure 1A). However, only one broad diffraction peak remains upon silica removal, suggesting that the long-range ordered mesostructure suffers from a little shrinkage. The TEM image with its FFT pattern provides a direct visualization of well-ordered arrays of mesoporous channels for $Ru_{0.9}Ni_{0.1}$−OMC (Figure 1A, inset). The high-energy X-ray diffraction pattern of $Ru_{0.9}Ni_{0.1}$−OMC provides broad but clear (101), (102), and (110) diffractions (Figure 2B), ascribed to the formation of finely hcp structured Ru−Ni bimetallic NPs.[32] Interestingly, $Ru_{0.7}Ni_{0.3}$−OMC exhibits characteristic (111), (200), (220), (311), and (222) diffractions, indicating the formation of fcc bimetallic nanocrystallites,[33−35] and these diffraction peaks shift to higher angles as the atomic percentage of Ru decreased for $Ru_{0.5}Ni_{0.5}$−OMC, demonstrating a lattice contraction originating from the substitution of the smaller Ni atoms in place of the larger Ru atoms. Correspondingly, the lattice constants based on (220) diffractions also decrease (Table S1).

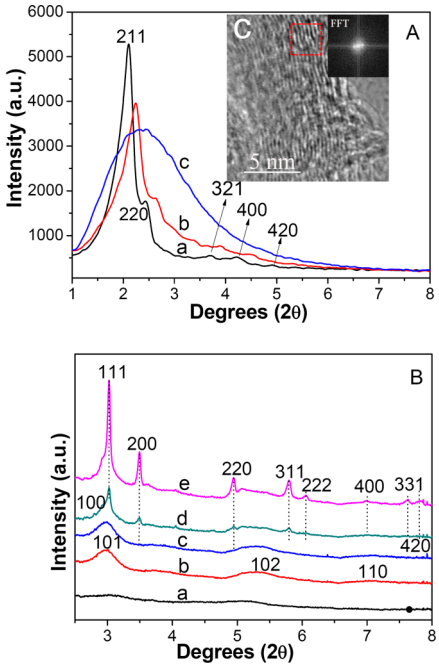

Figure 1. (A) Small angle X-ray diffraction with TEM (inset) and (B) high-energy X-ray diffraction patterns of (a) $Ru_{0.9}Ni_{0.1}$−C_{16}SC, (b) $Ru_{0.9}Ni_{0.1}$−OMSC, (c) $Ru_{0.9}Ni_{0.1}$−OMC, (d) $Ru_{0.7}Ni_{0.3}$−OMC, and (e) $Ru_{0.5}Ni_{0.5}$−OMC.

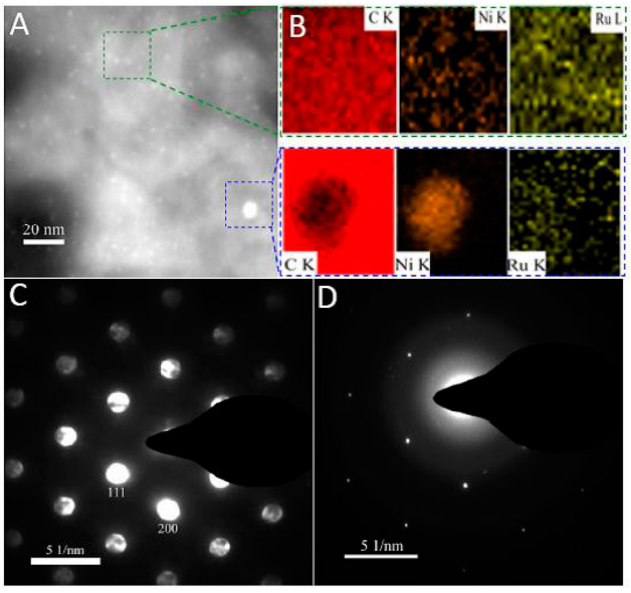

Figure 2. (A) The HAADF-STEM image for $Ru_{0.9}Ni_{0.1}$−OMC. (B) The corresponding carbon, nickel, and ruthenium elemental maps using EDX for large and small particles as marked in HAADF-STEM. (C) The electron microdiffraction pattern for single large particle in A. (D) The selected area electron diffraction (SAED) pattern for $Ru_{0.9}Ni_{0.1}$−OMC.

The embedded Ru−Ni bimetallic NPs can be directly discerned in the atomic resolution high-angle annular dark-field (HAADF) images. For $Ru_{0.9}Ni_{0.1}$−OMC, Figure 2A clearly shows homogeneously distributed bright spots, corresponding to highly dispersed large (5.2 ± 0.4 nm) and smaller (1.8 ± 0.2 nm) particles (Figure S7). The composition of both large and smaller particles was demonstrated by investigating carbon, nickel, and ruthenium elemental maps using EDX (Figure 2B).

dx.doi.org/10.1021/cs401030u | *ACS Catal.* 2014, 4, 1419−1425

It reveals that the large particle proves to be Ni-aggregated nanocrystallite with sporadic Ru inserted and around it, providing an *fm*3*m* symmetry confirmed by electron microdiffraction (Figure 2C), while the smaller one is Ru-rich NP, suggesting the formation of composition-tuned Ru−Ni bimetallic NPs. The selected area electron diffraction (SAED) pattern of $Ru_{0.9}Ni_{0.1}$−OMC mainly displays *hcp* features (Figure 2D). Similar to immiscible bimetals Au−Pt[36] and Ag−Rh[37] in bulk form alloyed on the nanoscale, trapping Ni and Ru into an alloyed particle is not easy, due to the large standard reduction-potential difference;[38] fortunately, it is facilely realized in our experiment through a fast *in situ* reduction process. Figure S7 shows the TEM images and the corresponding particle size distributions for Ru_xNi_{1-x}−OMC series. It is clear that all Ru_xNi_{1-x}−OMC samples exhibit both small and large NPs with a bimodal size distribution, bearing decreased average diameter for both large and small NPs as the atomic percentage of Ru increases. Correspondingly, high resolution TEM images exhibit an increased lattice separation as for the fringes in the (111) direction (Figure S8), confirming XRD findings.

To further verify the formation of alloyed Ru−Ni NPs in ordered mesoporpus carbons, metal-specific XAFS was measured *via* separated Ru and Ni K-edge scans. Herein, $Ru_{0.5}Ni_{0.5}$-containing samples are more representative owing to the similar content for bimetals. As illustrated in Figure 3A,

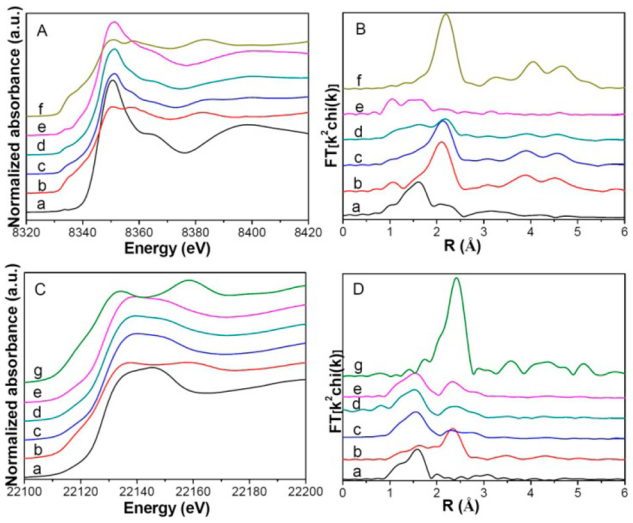

Figure 3. X-ray absorption near edge structure (XANES) of the Ni−K edge (A) and Ru−K edge (C), and the magnitude of the Fourier transforms (not corrected for phase shifts) of the k^2 weighted Ni−K edge (B) and Ru−K edge (D) EXAFS of (a) $Ru_{0.5}Ni_{0.5}$−C_{16}SC, (b) $Ru_{0.5}Ni_{0.5}$−OMSC, (c) $Ru_{0.5}Ni_{0.5}$−OMC, (d) $Ru_{0.7}Ni_{0.3}$−OMC, (e) $Ru_{0.9}Ni_{0.1}$−OMC, (f) Ni foil, and (g) Ru foil.

different from $Ru_{0.5}Ni_{0.5}$−C_{16}SC, $Ru_{0.5}Ni_{0.5}$−OMSC and $Ru_{0.5}Ni_{0.5}$−OMC exhibit a newly present pre-edge peak and negative shift in the adsorption edge position, suggesting that the Ni(+2) species are mostly reduced,[39,40] though they carry some positive charges because of a slightly positive shifted edge position as compared to the Ni reference.[41] In the corresponding *k* space, $Ru_{0.5}Ni_{0.5}$−OMSC and $Ru_{0.5}Ni_{0.5}$−OMC show clear oscillations at a higher *k* region of $k > 8$ Å^{-1} as compared to $Ru_{0.5}Ni_{0.5}$−C_{16}SC (Figure S9), indicating the dominance of high Z backscatters, which would be Ni or Ru. Consistently, $Ru_{0.5}Ni_{0.5}$−OMSC and $Ru_{0.5}Ni_{0.5}$−OMC exhibit one prominent peak at ∼2.1 Å from either the Ni−Ru or Ni−Ni contributions, different from ∼1.6 Å from the Ni−O pairs from $Ru_{0.5}Ni_{0.5}$−C16SC (Figure 3B), confirming the formation of alloyed Ru−Ni NPs.[42] As for Ru K-edge analysis, $Ru_{0.5}Ni_{0.5}$−OMC is more similar to $Ru_{0.5}Ni_{0.5}$−C_{16}SC in the XANES (Figure 3C), k^2-weighted EXAFS (Figure S10), and Fourier transformed EXAFS (*r* space, Figure 3D) features, rather than Ru foil. It can be ascribed to the dominance of low Z backscatters around Ru atoms, which would be O in our system,[43] revealing that the formed Ru(0) species were partially oxidized upon hot alkaline treatment. As for Ru_xNi_{1-x}−OMC series, exploration of the short-ranged structure from 1 to 3 Å is meaningful, since the local information may closely correlate with catalytic properties. As illustrated in Figure 3B,c−e, Ru_xNi_{1-x}−OMC series show the declined peak intensity around 2.1 Å as the molar percentage of Ru increases, ascribed to less Ru or Ni coordinated with central Ni atoms, also verified by Figure S11. On the contrary, there is an increased Ni−C contribution centered at 1.5 Å, suggesting the stronger metal−support interaction for composition-tuned $Ru_{0.9}Ni_{0.1}$−OMC. On the other hand, Ni content plays an insignificant role on the local structure of Ru (Figure S12). It is clear that Ru_xNi_{1-x}−OMC series exhibit identical Ru−O and Ru−Ru/Ni contributions at 1.5 and 2.3 Å,[44] respectively. These results indicate that Ru NPs prefer homogeneous nucleation to form small Ru-rich bimetallics with strong interaction with support, while Ni NPs prefer heterogeneous nucleation to form large Ni-rich NPs.

FT-IR spectra are also sensitive to the change that occurred during the synthetic process. $Ru_{0.9}Ni_{0.1}$−C_{16}SC shows the characteristic C−H stretching from the CTA+ fragment at 2927 and 2855 cm^{-1}, pyridyl and aromatic ring vibrations between 1600 and 1300 cm^{-1}, as well as silica framework vibration mode at 1085 and 465 cm^{-1} (Figure S13), confirming that CTS-HQ and silica have been incorporated into the CTAB-directed $Ru_{0.9}Ni_{0.1}$−C_{16}SC mesophase.[45−47] However, only characteristic silica peaks remain upon pyrolysis, suggesting that surfactant removal and CTS-HQ carbonization occurred. Further silica removal is supported by the disappearance of silica peaks after alkaline etching. We conducted elemental analysis (C, H, and N) of $Ru_{0.9}Ni_{0.1}$−OMC, $Ru_{0.7}Ni_{0.3}$−OMC, and $Ru_{0.5}Ni_{0.5}$−OMC; their N content ranged from 1.6 to 1.9 wt %, and no obvious difference was observed.

Simultaneously, pyrolysis followed by silica removal creates mesoporous structures. N_2 adsorption reveals a IV type isotherm with a distinct H1 type hysteresis loop for $Ru_{0.9}Ni_{0.1}$−OMSC and $Ru_{0.9}Ni_{0.1}$−OMC (Figure 4A), confirming mesoporous materials with slit pores.[48,49] Upon silica removal, the pore size slightly increases by 2.1%, while the specific surface area and pore volume increase dramatically, nearly double those of $Ru_{0.9}Ni_{0.1}$−OMSC (Table S2). The S_{meso}/S_{micro} ratio and V_{meso}/V_{micro} ratio decrease from 0.79 to 0.56 and from 2.35 to 1.89, suggesting more microstructures were formed upon silica removal. As for Ru_xNi_{1-x}−OMC series, it is observed that the surface area and pore volume enhance with the increase of ruthenium content, probably because of more small Ru-rich bimetallic NP formation. Notably, all Ru_xNi_{1-x}−OMC samples show narrow pore size distribution (Figure 4B) centered at ca. 4.30 nm.

The hydrogenation of LA to GVL was chosen as a probe reaction to investigate the catalytic performances of Ru_xNi_{1-x}−OMC series, since GVL has been identified as a platform molecule from renewable biomass with wide application in

dx.doi.org/10.1021/cs401030u | ACS Catal. 2014, 4, 1419−1425

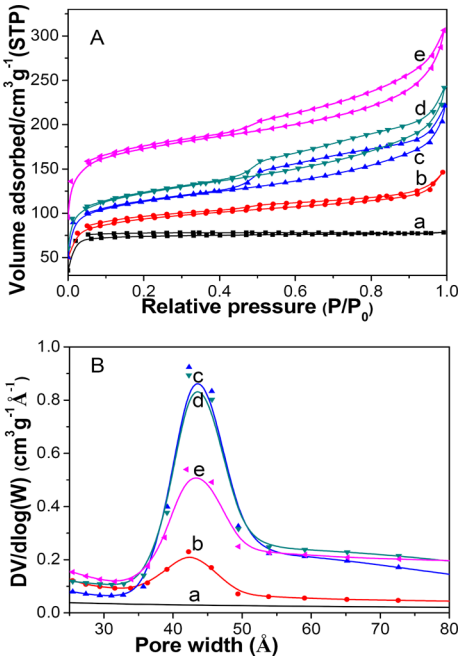

Figure 4. (A) N_2 adsorption/desorption isotherms and (B) pore size distribution profiles of (a) $Ru_{0.9}Ni_{0.1}$−C, (b) $Ru_{0.9}Ni_{0.1}$−OMSC, (c) $Ru_{0.9}Ni_{0.1}$−OMC, (d) $Ru_{0.7}Ni_{0.3}$−OMC, and (e) $Ru_{0.5}Ni_{0.5}$−OMC.

chemical synthesis and liquid transportation fuels. It has been proved that the introduction of a heterometal species into Ru/C could enhance its catalytic performance,[15,16] since the formation of bimetallic NPs is beneficial to the homogeneous dispersion of smaller Ru NPs and enhances their interaction with the carbonaceous support, which was also herein detected by the in-depth characterization of the present Ru_xNi_{1-x}−OMC catalysts. The selected results on Ru_xNi_{1-x}−OMC catalyzed LA hydrogenation are summarized in Table 1; as expected, the

Table 1. Catalytic Hydrogenation of LA with Different Catalysts[a]

		metal loading (mmol g^{-1})				
entry	catalyst	Ni	Ru	LA conversion (%)	GVL yield (%)	TOF[b] (h^{-1})
1	OMC			6		
2	$Ru_{0.5}Ni_{0.5}$−OMC	0.4363	0.3424	45	41	1716
3	$Ru_{0.7}Ni_{0.3}$−OMC	0.2683	0.4589	96	94	2936
4	$Ru_{0.9}Ni_{0.1}$−OMC	0.0817	0.5557	99	97	2501
5	Ru−OMC		0.6076	99	97	2288
6	$Ru_{0.9}Ni_{0.1}$−OMSC	0.0532	0.4302	39	36	1199
7	$Ru_{0.9}Ni_{0.1}$−C	0.0717	0.5045	34	15	426
8	commercial Ru/C		0.4940	48	30	870
9[c]	$Ru_{0.9}Ni_{0.1}$−OMC	0.0817	0.5557	97	84	2167

[a]Reaction conditions: LA, 5.0 g (43 mmol); catalyst, 0.3 wt % (15 mg); H_2, 4.5 MPa; 2 h; and 423 K. [b]TOF, h^{-1} (turnover frequency): moles of GVL produced per Ru mole metal ion per hour. [c]LA, 2.0 g (17.2 mmol); catalyst, 0.3 wt % (6 mg); H_2O, 3.0 g; H_2, 4.5 MPa; 2 h; and 423 K.

blank OMC support exhibits insignificant LA conversion owing to the absence of active sites (entry 1). All Ru_xNi_{1-x}−OMC samples (0.3 wt %) were active toward the catalytic hydrogenation of 5.0 g of LA under 4.5 MPa of H_2 at 150 °C for 2 h, affording high selectivity to GVL without any solvent. It is interesting that the LA conversion and GVL yield are improved with the increase in Ru composition (entries 2−4), while the Ni/C with 3.3 wt % Ni loading only provided 3% yield of GVL under the same reaction conditions, suggesting that the Ru species is the main active component. $Ru_{0.7}Ni_{0.3}$−OMC afforded a 94% yield of GVL with a TOF value as high as 2936 h^{-1} (entry 3); $Ru_{0.9}Ni_{0.1}$−OMC and Ru−OMC all gave near quantitative LA conversions with the TOF value attaining 2501 h^{-1} and 2288 h^{-1} (entries 4 and 5), respectively. These three catalysts are much more active than that of $Ru_{0.5}Ni_{0.5}$−OMC and commercial Ru/C (entry 8). Considering that LA aqueous solutions could be directly obtained from the acid-catalyzed conversion of biomass, water was then explored as a potential solvent using $Ru_{0.9}Ni_{0.1}$−OMC as the representative catalyst, and a similar LA conversion (97%) but lower GVL yield (84%) were obtained under the same catalyst loading with that over $Ru_{0.9}Ni_{0.1}$−OMC, suggesting such Ru_xNi_{1-x}−OMC could also work smoothly for the aqueous LA solution (entry 9).

It is known that the textural properties of the catalyst also affect its catalytic performances significantly. $Ru_{0.9}Ni_{0.1}$−C, prepared as a comparison via directpyrolysis of a chitosan−ruthenium−nickel coordination polymer (see Supporting Information), lacks a uniform mesopore distribution (Figure 4a) and exhibits a much lower LA conversion of 34% with a trace GVL yield (entry 7), suggesting that the mesoporous arrays also play an important role in achieving high catalytic activity and selectivity. Mesoporous $Ru_{0.9}Ni_{0.1}$−OMSC showed moderate GVL yield (entry 6), and then its yield could be readily improved to 97% over $Ru_{0.9}Ni_{0.1}$−OMC; this obvious activity difference indicates that the larger surface areas and pore volumes are essential to enhancing the catalytic efficiency as well. It is concluded that $Ru_{0.9}Ni_{0.1}$−OMC showed the best catalytic performances of any catalysts in this study, which highly depended on the homogeneously dispersed small Ru-rich NPs and the ordered mesoporous arrays with large surface area and pore volumes; all of these physicochemical properties may facilitate the LA adsorption and GVL diffusion well.

Besides the efficient catalytic activity, stable recyclability is also crucial for an outstanding heterogeneous catalyst from the viewpoint of both academic research and industrial applications. As for LA hydrogenation, traditional Ru/C has been proved to be one of the most active catalysts so far. However, Liu et al. found that the initial 99% conversion of LA catalyzed commercial Ru/C dropped to 42% in the fourth reuse.[13] As illustrated in Figure 5, $Ru_{0.7}Ni_{0.3}$−OMC lost 13% of GVL yield after six cycles, while $Ru_{0.9}Ni_{0.1}$−OMC was quite stable and could be used at least 15 times without a significant loss of activity. To further verify its stability, the Ru concentration in the reaction solution was checked by ICP-AES to be negligible leaching of Ru species into the liquid phase. The HAADF STEM image of the spent $Ru_{0.9}Ni_{0.1}$−OMC (Figure S14) shows less agglomeration after 15 times usage as compared with that of $Ru_{0.7}Ni_{0.3}$−OMC after being recycled six times; therefore it still exhibits 90% of GVL yield. As far as we know, as the prepared $Ru_{0.9}Ni_{0.1}$−OMC catalyst is the most stable Ru-based heterogeneous catalyst reported in the LA hydrogenation, and its robust nature can be ascribed to the

dx.doi.org/10.1021/cs401030u | ACS Catal. 2014, 4, 1419−1425

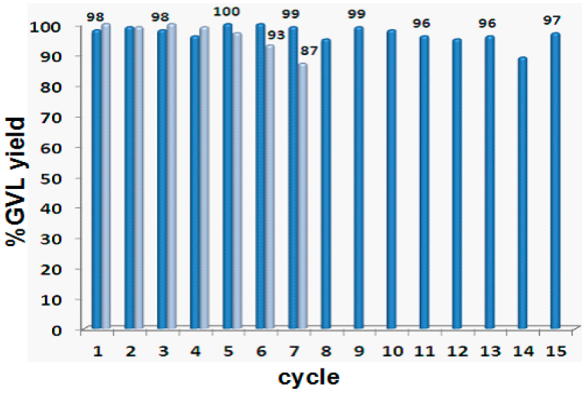

Figure 5. Recyclability test for $Ru_{0.9}Ni_{0.1}$−OMC (blue) and $Ru_{0.7}Ni_{0.3}$−OMC (gray). Reaction conditions: LA (5.0 g), catalyst (15 mg), H_2 (4.5 MPa), 423 K, and 2 h.

enhanced interaction of embedded small Ru−Ni bimetallic NPs with the carbonaceous support, as revealed by advanced electron microscopy.[50] This strong metal support interaction can also be demonstrated by the presence of Ni−C pairs (ca. 1.5 Å) in $Ru_{0.9}Ni_{0.1}$−OMC (Figure 3B,e). To make the hydrogenation of LA yield of GVL commercially competitive, the development of a highly acitive and stable catalyst that is also the main limitation of the reported examples[50,51] is among the biggest challenges. Herein, the elaborately composition-tuned $Ru_{0.9}Ni_{0.1}$−OMC catalyst provided an alternative.

4. CONCLUSION

In summary, facile fabrication of composition-tuned Ru−Ni bimetallics homogeneously dispersed in ordered mesoporous carbons has been successfully achieved by constructing a CTAB-directed chitosan−ruthenium−nickel−silica mesophase before pyrolysis and silica removal. Deep investigation reveals that the catalytic performance highly depends on both Ru−Ni bimetallics and carbonaceous supports, as well as their ensemble effect, verified by various characterization techniques and a comparative catalytic test. The elaborately tuned $Ru_{0.9}Ni_{0.1}$−OMC catalysts demonstrated unprecedented catalytic activity and stability for the catalytic hydrogenation of LA to GVL, ascribing to the homogeneous embedding of Ru−Ni bimetallics in a mesoporous carbonaceous matrix with a strong metal−support interaction. The development of such efficient Ru−Ni bimetallic mesoporous carbons successfully proves the concept of composition-tuned multicomponent assembly and also gives a strong indication of its generality in the facile fabrication of a variety of heterogeneous bi- and/or trimetallic OMCs through this step-economic multicomponent assembly procedure.

■ ASSOCIATED CONTENT

Supporting Information

The details of the preparation of materials and their characterization. This information is available free of charge via the Internet at http://pubs.acs.org/.

■ AUTHOR INFORMATION

Corresponding Author

*E-mail: fuweili@licp.cas.cn.

Notes

The authors declare no competing financial interest.

■ ACKNOWLEDGMENTS

Financial support from the Chinese Academy of Sciences, the National Natural Science Foundation of China (21373246, 21303229, and 21173269), and the Science Foundation of China University of Petroleum, Beijing (2462013YJRC018) is greatly appreciated. The proposals (GUP28010 and GUP31195) given by Advanced Photon Source of the Office of Science, U.S. Department of Energy under Contract DE-AC02-06CH11357 are acknowledged. We also thank Prof. Haichao Liu and Dr. Junfang Nie for their help in the ICP-AES analysis.

■ REFERENCES

(1) Wei, Z. H. *Chem. Soc. Rev.* **2012**, *41*, 7994−8008.
(2) Yu, W.; Porosoff, M. D.; Chen, J. G. G. *Chem. Rev.* **2012**, *112*, 5780−5817.
(3) Kellya, T. G.; Chen, J. G. G. *Chem. Soc. Rev.* **2012**, *41*, 8021−8034.
(4) Guczi, L. *Catal. Today* **2005**, *101*, 53−64.
(5) Lee, J.; Kim, J.; Hyeon, T. *Adv. Mater.* **2006**, *18*, 2073−2094.
(6) Pang, J. F.; Wang, A. Q.; Zheng, M. Y.; Zhang, Y. H.; Huang, Y. Q.; Chen, X. W.; Zhang, T. *Green Chem.* **2012**, *14*, 614−617.
(7) Liu, X. Y.; Wang, A. Q.; Wang, X. D.; Mou, C.-Y.; Zhang, T. *Chem. Commun.* **2008**, 3187−3189.
(8) Witham, C. A.; Huang, W.; Tsung, C. K.; Kuhn, J. N.; Somorjai, G. A.; Toste, F. D. *Nat. Chem.* **2010**, *2*, 36−41.
(9) Fulvio, P. F.; Liang, C. D.; Dai, S.; Jaroniec, M. *Eur. J. Inorg. Chem.* **2009**, 605−612.
(10) Li, X. Y.; Wang, X.; Song, S. Y.; Liu, D. P.; Zhang, H. J. *Chem.—Eur. J.* **2012**, *18*, 7601−7607.
(11) Wright, W. R. H.; Palkovits, R. *ChemSusChem* **2012**, *5*, 1657−1667.
(12) Li, W.; Xie, J.-H.; Lin, H.; Zhou, Q.-L. *Green Chem.* **2012**, *14*, 2388−2390.
(13) Yan, Z.-P.; Lin, L.; Liu, S. J. *Energy Fuels* **2009**, *23*, 3853−3858.
(14) Galletti, A. M. R.; Antonetti, C.; Luise, V. D.; Martinelli, M. A. *Green Chem.* **2012**, *14*, 688−694.
(15) Braden, D. J.; Henao, C. A.; Heltzel, J.; Maravelias, C. C.; Dumesic, J. A. *Green Chem.* **2011**, *13*, 1755−1765.
(16) Alonso, D. M.; Wettstein, S. G.; Bond, J. Q.; Root, T. W.; Dumesic, J. A. *ChemSusChem* **2011**, *4*, 1078−1081.
(17) Li, Z. L.; Liu, J. H.; Huang, Z. W.; Yang, Y.; Xia, C. G.; Li, F. W. *ACS Catal.* **2013**, *3*, 839−845.
(18) Ma, S. Q.; Goenaga, G. A.; Call, A. V.; Liu, D.-J. *Chem.—Eur. J.* **2011**, *17*, 2063−2067.
(19) Ma, T.-Y.; Liu, L.; Yuan, Z.-Y. *Chem. Soc. Rev.* **2013**, *42*, 3977−4003.
(20) Wan, Y.; Shi, Y. F.; Zhao, D. Y. *Chem. Mater.* **2008**, *20*, 932−945.
(21) Deng, Y. H.; Yu, T.; Wan, Y.; Shi, Y. F.; Meng, Y.; Gu, D.; Zhang, L. J.; Huang, Y.; Liu, C.; Wu, X. J.; Zhao, D. Y. *J. Am. Chem. Soc.* **2007**, *129*, 1690−1697.
(22) Liu, R. L.; Shi, Y. F.; Meng, Y.; Zhang, F. Q.; Gu, D.; Chen, Z. X.; Tu, B.; Zhao, D. Y. *J. Am. Chem. Soc.* **2006**, *128*, 11652−11662.
(23) Li, Z. L.; Liu, J. H.; Xia, C. G.; Li, F. W. *ACS Catal.* **2013**, *3*, 2440−2448.
(24) Ryoo, R.; Joo, S. H.; Kruk, M.; Jaroniec, M. *Adv. Mater.* **2001**, *13*, 677−681.
(25) Liu, F. Y.; Carlos, L. D.; Ferreira, R. A. S.; Rocha, J.; Ferro, M. C.; Tourrette, A.; Quignard, F.; Robitzer, M. *J. Phys. Chem. B* **2010**, *114*, 77−83.
(26) Guibal, E. *Prog. Polym. Sci.* **2005**, *30*, 71−109.
(27) Huang, J. H.; Tian, G.; Wang, H. S.; Xu, L.; Kan, Q. B. *J. Mol. Catal. A: Chem.* **2007**, *271*, 200−208.
(28) Kleitz, F.; Choi, S. H.; Ryoo, R. *Chem. Commun.* **2003**, 2136−2137.

(29) Liu, X. Y.; Tian, B. Z.; Yu, C. Z.; Gao, F.; Xie, S. H.; Tu, B.; Che, R. C.; Peng, L.-M.; Zhao, D. Y. *Angew. Chem., Int. Ed.* **2002**, *41*, 3876−3878.
(30) Liang, C. D.; Li, Z. J.; Dai, S. *Angew. Chem, Int. Ed.* **2008**, *47*, 3696−3717.
(31) Wan, Y.; Zhao, D. Y. *Chem. Rev.* **2007**, *107*, 2821−2860.
(32) Viau, G.; Brayner, R.; Poul, L.; Chakroune, N.; Lacaze, E.; Fiévet-Vincent, F.; Fiévet, F. *Chem. Mater.* **2003**, *15*, 486−494.
(33) Chen, G. Z.; Desinan, S.; Nechache, R.; Rosei, R.; Rosei, F.; Ma, D. L. *Chem. Commun.* **2011**, *47*, 6308−6310.
(34) Chen, G. Z.; Desinan, S.; Rosei, R.; Rosei, F.; Ma, D. L. *Chem.—Eur. J.* **2012**, *18*, 7925−7930.
(35) Chen, L.; Chen, J. M.; Zhou, H. D.; Zhang, D. J.; Wan, H. Q. *Mater. Sci. Eng., A* **2007**, *452*−*453*, 262−266.
(36) Zhou, S. H.; Jackson, G. S.; Eichhorn, B. *Adv. Funct. Mater.* **2007**, *17*, 3099−3104.
(37) Kim, J.; Lee, Y. M.; Sun, S. H. *J. Am. Chem. Soc.* **2010**, *132*, 4996−4997.
(38) Braos-García, P.; García-Sancho, C.; Infantes-Molina, A.; Rodríguez-Castellón, E.; Jiménez-López, A. *Appl. Catal. A: Gen.* **2010**, *381*, 132−144.
(39) Sarma, L. S.; Chen, C.-H.; Kumar, S. M. S.; Wang, G.-R.; Yen, S.-C.; Liu, D.-G.; Sheu, H.-S.; Yu, K.-L.; Tang, M.-T.; Lee, J.-F.; Bock, C.; Chen, K.-H.; Hwang, B.-J. *Langmuir* **2007**, *23*, 5802−5809.
(40) Daniel, O. M.; DeLaRiva, A.; Kunkes, E. L.; Datye, A. K.; Dumesic, J. A.; Davis, R. J. *ChemCatChem* **2010**, *2*, 1107−1114.
(41) Sun, S. H.; Zhang, G. X.; Gauquelin, N.; Chen, N.; Zhou, J. G.; Yang, S. L.; Chen, W. F.; Meng, X. B.; Geng, D. S.; Banis, M. N.; Li, R. Y.; Ye, S. Y.; Knights, S.; Botton, G. A.; Sham, T.-K.; Sun, X. L. *Sci. Rep.* **2013**, *3*, 1−9.
(42) Li, D. L.; Atake, I.; Shishido, T.; Oumi, Y.; Sano, T.; Takehira, K. *J. Catal.* **2007**, *250*, 299−312.
(43) Qiao, B. T.; Wang, A. Q.; Yang, X. F.; Allard, L. F.; Jiang, Z.; Cui, Y. T.; Liu, J. Y.; Li, J.; Zhang, T. *Nat. Chem.* **2011**, *3*, 634−641.
(44) Zaikovskii, V. I.; Nagabhushana, K. S.; Kriventsov, V. V.; Loponov, K. N.; Cherepanova, S. V.; Kvon, R. I.; Bo1nnemann, H.; Kochubey, D. I.; Savinova, E. R. *J. Phys. Chem. B* **2006**, *110*, 6881−6890.
(45) Gallo, J. M. R.; Pastore, H. O.; Schuchardt, U. *J. Catal.* **2006**, *243*, 57−63.
(46) Maurya, M. R.; Sikarwar, S. *J. Mol. Catal. A: Chem.* **2007**, *263*, 175−185.
(47) Maurya, M. R.; Chandrakar, A. K.; Chand, S. *J. Mol. Catal. A: Chem.* **2007**, *270*, 225−235.
(48) Corma, A. *Chem. Rev.* **1997**, *97*, 2373−2419.
(49) Robles-Dutenhefner, P. A.; Rocha, K. A. D.; Sousa, E. M. B.; Gusevskaya, E. V. *J. Catal.* **2009**, *265*, 72−79.
(50) Zhou, W. P.; Lewera, A.; Larsen, R.; Masel, R. I.; Bagus, P. S.; Wieckowski, A. *J. Phys. Chem. B* **2006**, *110*, 13393−13398.
(51) Yu, X.; Pickup, P. G. *J. Power Sources* **2008**, *182*, 124−132.